

## Research Article

# One-step solvothermal preparation of Fe-doped Ni<sub>0.85</sub>Se/NF: An efficient catalyst for the oxygen evolution reaction

Longqi Zhu<sup>a,#</sup>, Runze Wang<sup>a,#</sup>, Chen Wang<sup>a</sup>, Shuhan Yang<sup>a</sup>, Haizhen Liu<sup>b</sup>, Bo Xing<sup>c</sup>,  
 Honghui Cheng<sup>d</sup>, Kuikui Wang<sup>a,e,\*</sup>

<sup>a</sup> Institute of Materials for Energy and Environment, Laboratory of New Fiber Materials and Modern Textile, Growing Basis for State Key Laboratory, College of Materials Science and Engineering, Qingdao University, Qingdao 266071, China

<sup>b</sup> MOE Key Laboratory of New Processing Technology for Non-ferrous Metals and Materials, Guangxi Key Laboratory of Processing for Non-ferrous Metals and Featured Materials, Guangxi University, Nanning 530004, China

<sup>c</sup> National Engineering Laboratory of Circular Economy, Sichuan University of Science and Engineering, Zigong 643000, China

<sup>d</sup> School of Mechanical Engineering, Yangzhou University, Yangzhou 225127, China

<sup>e</sup> Jiangsu Key Laboratory of Advanced Catalytic Materials and Technology, Changzhou University, Changzhou 213164, China

## ARTICLE INFO

## Keywords:

Doping  
 Selenylation  
 Hydrothermal reaction  
 Oxygen evolution reaction  
 Electrocatalysts

## ABSTRACT

Metal–cation doping is a fundamental strategy for enhancing catalyst performance. Fe-doped Ni<sub>0.85</sub>Se/NF (Fe-Ni<sub>0.85</sub>Se/NF) nanoparticles were prepared at 80 °C via Fe<sup>2+</sup> etching method. The addition of Fe altered the coordination environment of the Ni species along with the catalyst's morphology, creating additional active sites. Notably, the synergistic interaction between the bimetallic components augmented the built-in activity and accelerated reaction kinetics. The Fe-Ni<sub>0.85</sub>Se/NF electrocatalysts demonstrated remarkable catalytic activity for the oxygen evolution reaction (OER), with an acceptable overpotential of 276 mV and a Tafel slope of 58.1 mV dec<sup>-1</sup> at 100 mA cm<sup>-2</sup>. Moreover, they demonstrated exceptional durability. In situ Raman and X-ray photoelectron spectroscopy (XPS) analyses showed that the excellent OER performance stemmed from the reconstruction-induced hydroxyl oxide. This study offers a novel approach for streamlining the synthesis procedures and reducing the experimental costs for developing high-efficiency electrocatalysts.

## 1. Introduction

Energy and pollution pose significant challenges to sustainable human existence [1–5]. Since the beginning of the 21st century, researchers have focused on developing renewable energy sources to replace traditional, high-pollution options [6–9]. Hydrogen preparation by electrolytic water has become a potential green energy source because of its high conversion efficiency and environmental compatibility [10–13]. Water splitting involves two half-reactions [14–16], which, however, exhibit sluggish kinetics (especially the oxygen evolution reaction (OER) involving a four-electron process), thus bottlenecking water electrolysis [17–19]. Although noble metal catalysts such as Pt, RuO<sub>2</sub>, and IrO<sub>2</sub> have been utilized to produce hydrogen on an industrial scale, their scarcity and high cost restrict their widespread use and scalability [20–22]. Hence, developing affordable and highly effective non-noble-metal OER catalysts remains a crucial research goal.

Transition metal hydroxides, phosphates, and chalcogenides have garnered significant interest because of their straightforward synthesis

and exceptional catalytic activity [23–28]. Non-stoichiometric nickel-selenium compounds show excellent OER activity owing to their high intrinsic activity and adjustable properties [29–31]. In addition, their activity can be further enhanced when Ni–Se compounds are doped with other cations [32–35]. Various studies have shown that metal cation-doped nickel-selenium compounds exhibit excellent activity and stability in the OER [36–40]. Liang et al. reported Co-doped NiSe nanoflowers deposited in situ on Ni foam (NF) substrates, which exhibited excellent catalytic performance for the OER, with an overpotential of 380 mV at a current density of 100 cm<sup>-2</sup> [36]. Wang et al. used first-principles calculations to investigate the influence of metal cation doping on the catalytic performance of NiSe<sub>2</sub>, with the results confirming that Fe was the best candidate for regulating NiSe<sub>2</sub> [37]. Similarly, Chang et al. synthesized a novel three-dimensional hierarchical network on a carbon paper substrate with a high OER performance using 2D Fe-doped NiSe and carbon nanotubes, demonstrating that the synergistic effect of Fe doping predominantly enhanced the catalytic activity [38]. Liu et al. used a one-step solvothermal approach to produce Ni<sub>0.85</sub>Se on an NF substrate.

\* Corresponding author.

E-mail address: [kkwang@qdu.edu.cn](mailto:kkwang@qdu.edu.cn) (K. Wang).

# These authors contributed equally to this work.

By doping various quantities of Fe to control the morphology and electrochemical properties of Ni<sub>0.85</sub>Se, the optimized Fe-Ni<sub>0.85</sub>Se exhibited outstanding hydrogen evolution reaction (HER) and OER properties and could be employed for total water decomposition. This outstanding performance was attributed to the unique 2D nanosheet array structure, high conductivity, and enlarged electroactive area induced by Fe doping [39]. Despite the high catalytic activity of Fe-doped nickel-selenium compounds, the majority of them are prepared in a high-temperature environment by adding nickel salt and a reducing agent, thereby producing toxic gases and pollutive by-products that detrimentally impact the green development of energy.

On this basis, we herein propose a simple low-temperature hydrothermal strategy for the synthesis of Fe-doped Ni<sub>0.85</sub>Se (Fe-Ni<sub>0.85</sub>Se) electrocatalysts. SeO<sub>2</sub> was utilized as the Se source without relying on a reductant to mitigate pollutant introduction, and an NF substrate was employed as the nickel source. Notably, the etching of Fe ions dramatically decreased the synthesis temperature required in our approach, yielding a low-crystallinity catalyst exhibiting excellent OER activity and stability in 1 M KOH electrolyte. Specifically, an overpotential of 276 mV was achieved at a 100 mA cm<sup>-2</sup> current density, surpassing the reported performances of catalysts like Ni<sub>0.85</sub>Se without Fe doping and commercial RuO<sub>2</sub> under the same load and operation conditions. Furthermore, our catalyst exhibited long-term electrochemical stability, with negligible performance degradation during a 100 h OER test. We prospect for the findings reported herein to pave the way for the development of highly efficient electrolytic water catalysts.

## 2. Results and discussion

Granular Fe-Ni<sub>0.85</sub>Se was synthesized using a one-step hydrothermal process with NF and SeO<sub>2</sub>, respectively, as Ni source and Se sources. A typical synthesis strategy is illustrated in Fig. 1(a). After 4 h of low-temperature hydrothermal treatment without Fe doping, two different morphologies were realized on the NF substrate surface (Figs. 1(b)–(d)) in the scanning electron microscopy (SEM) images: one with a diameter of approximately 1 μm and a relatively smooth surface, and the other with a diameter of approximately 200 nm and a rough surface resembling that of frill. Energy-dispersive X-ray (EDS) elemental mappings elemental mapping was performed to determine further the chemical composition of Ni<sub>0.85</sub>Se/NF (Fig. S1). The bulk of Se was observed to cluster on the large and smooth particles in the middle, whereas Ni and the remaining Se were clustered on the surrounding folded particles. This indicated the excessive presence of SeO<sub>2</sub> during the reaction. However, the morphology of the catalyst changed after doping with 0.4 mmol Fe (Figs. 1(e)–(g)). Particles, approximately 400 nm in size, were homogeneously supported on the NF surface. Additional smaller particles existed atop the surface of the larger particles, contributing to the surface's roughness, which was conducive to exposing more active sites. The presence of Fe was verified through EDS elemental mapping (Figs. 1(h)–(k)), which showed an even distribution of Ni and Se in contrast to the relatively sparse distribution of Fe. Combined with the X-ray diffraction (XRD) results (Fig. S1), no Fe peak was observed, demonstrating the successful doping of Fe.

The transmission electron microscopy (TEM) images in Figs. 2(a)–(e) further verified the structure of Fe-Ni<sub>0.85</sub>Se/NF. The particle size distribution was uniform (approximately 400 nm), with numerous small particles revealed upon further magnification. No apparent lattice was observed after magnification at 600000× (Fig. 2(e)). This was attributed to the low temperature and short synthesis time inhibiting the complete growth of the crystal structure, which was in accordance with the XRD low-intensity diffraction peak (Fig. 3(a)). In addition, electron diffraction analysis was performed on the material (Fig. 2(f)). The weak diffraction rings corresponded to the (102) and (101) crystal planes of Ni<sub>0.85</sub>Se, with no discernible diffraction rings assigned to Fe.

The effects of different temperatures and Fe<sup>2+</sup> doping levels on the phase composition of the catalyst were investigated. The X-ray

diffraction patterns of the catalysts are presented in Figs. S2(a)(b) (Fe<sub>x</sub>-Ni<sub>0.85</sub>Se/NF-Y, where x represents the amount of Fe<sup>2+</sup> doping (mmol), and Y represents the hydrothermal temperature). The Fe<sub>x</sub>-Ni<sub>0.85</sub>Se/NF-60 sample did not exhibit a distinct Ni<sub>0.85</sub>Se peak, while the intensity of the Ni<sub>0.85</sub>Se peak increased as the temperature rose. Similarly, the Ni<sub>0.85</sub>Se peak became more pronounced as the Fe<sup>2+</sup> concentration increased under a constant temperature. Notably, the diffraction peak of Ni<sub>0.85</sub>Se could hardly be observed when there was no Fe doping (Fig. 3(a)). This could be attributed to the release of Ni<sup>2+</sup> from the Ni foam driven by the etching effect of Fe<sup>2+</sup> during the hydrothermal process, which lowered the energy barrier of Ni<sub>0.85</sub>Se formation [41,42]. The elemental states and electronic interactions of the optimized catalysts were determined via X-ray photoelectron spectroscopy (XPS) analysis. Fig. 3(b) illustrates the total XPS spectra of Ni<sub>0.85</sub>Se/NF-80 and a typical Fe-Ni<sub>0.85</sub>Se/NF sample. Compared to Fe-Ni<sub>0.85</sub>Se/NF equivalent, the Ni 2p peak of Ni<sub>0.85</sub>Se/NF was weak, with no discernible Fe 2p peak. This further corroborates that the introduction of Fe facilitates the etching of metallic Ni on the NF surface [42], inducing the release of Ni<sup>2+</sup> and the decrease of the energy barrier for the synthesis of Ni<sub>0.85</sub>Se. Parallely, the XPS results revealed a weak Fe 2p peak, indicating the successful doping of Fe. In the high-resolution Fe 2p XPS spectrum of Fe-Ni<sub>0.85</sub>Se/NF (Fig. 3(c)), the peaks at 709.56 and 722.81 eV were assigned to the 2p<sub>3/2</sub> and 2p<sub>1/2</sub> states of Fe<sup>2+</sup>. The other two peaks at 711.6 and 724.89 eV corresponded to the 2p<sub>3/2</sub> and 2p<sub>1/2</sub> states of Fe<sup>3+</sup>. The presence of Fe<sup>3+</sup> was caused by the partial oxidation of Fe<sup>2+</sup> during the hydrothermal process. In addition, the peaks at 716.88 and 731.71 eV were attributed to satellite peaks (denoted "Sat."). The Ni 2p XPS profile of Ni<sub>0.85</sub>Se/NF is shown in Fig. 3(d). The peaks at 854.01 and 870.98 eV corresponded to the 2p<sub>3/2</sub> and 2p<sub>1/2</sub> states of Ni<sup>2+</sup>, while the peaks at 855.9 and 873.31 eV were attributed to Ni<sup>3+</sup>. Further, the peak at 862.2 eV was attributed to the satellite peaks [43]. With Ni<sub>0.85</sub>Se/NF-80 as a reference, after Fe doping, the Ni<sup>2+</sup> 2p<sub>3/2</sub> and Ni<sup>3+</sup> 2p<sub>3/2</sub> peaks negatively shifted by 0.82 and 0.44 eV, respectively, indicative of the high charge density of Fe [44]. The Se 3d spectrum (Fig. 3(e)) showed a peak at 58.93 eV, attributable to the oxidation state of Se, while the peaks at 54.55 and 55.53 eV corresponded to the 3d<sub>5/2</sub> and 3d<sub>3/2</sub> states of Se. Notably, the Se 3d<sub>5/2</sub> peak negatively shifted by 0.9 eV after Fe doping. The XPS results further confirmed the successful synthesis of Fe-doped Ni<sub>0.85</sub>Se. Meanwhile, Fig. 3(f) shows the in-situ Raman spectra of the OER process under varying potentials (1.0–1.9 V) in an alkaline solution. The strong peak observed from 1.0 to 1.4 V at ~681 cm<sup>-1</sup> was attributed to Ni-OH. When the potential reached 1.4 V, oxygen evolution was stimulated, and the Raman band for Ni-OH decreased; however, when the potential approached 1.6 V, the peaks of the δ (O–M–O) and ν (O–M–O) vibrations at ~604 and ~803 cm<sup>-1</sup>, respectively, increased. Concurrently, peaks at ~443 and ~492 cm<sup>-1</sup>, attributed to NiOOH, appeared and increased. The peak that appeared at 1072 cm<sup>-1</sup> was assigned to MOO<sup>-</sup>. Overall, the above results demonstrate that under alkaline conditions, the OER kinetics when employing the Fe-Ni<sub>0.85</sub>Se/NF electrocatalyst is directly tied to the reconstruction-induced hydroxyl oxide.

The OER performance of the catalyst was investigated using a typical three-electrode setup in a 1 M KOH electrolyte. As shown by the linear sweep voltammetry (LSV) curves (Fig. 4(a)), the optimized Fe-Ni<sub>0.85</sub>Se/NF configuration demonstrated the best catalytic performance, with overpotentials of 261, 276, and 307 mV under current densities of 50, 100, and 300 mA cm<sup>-2</sup>, respectively. The optimized Fe-Ni<sub>0.85</sub>Se/NF catalyst outperformed its Ni<sub>0.85</sub>Se/NF and commercial RuO<sub>2</sub>/NF analogs regarding electrocatalytic OER performance under the same loading mass. In general, a smaller Tafel slope reflects better kinetic properties (Fig. 4(b)). Obviously, the Tafel slope value of the optimized Fe-Ni<sub>0.85</sub>Se/NF (58.1 mV dec<sup>-1</sup>) was below those of Ni<sub>0.85</sub>Se/NF (76.2 mV dec<sup>-1</sup>) and RuO<sub>2</sub>/NF (146.6 mV dec<sup>-1</sup>). Fig. 4(h) confirms that the optimized Fe-Ni<sub>0.85</sub>Se/NF has the lowest overpotential and Tafel slope compared with other catalysts and commercial RuO<sub>2</sub>, approximating the values of equivalent recently reported OER catalysts (Table

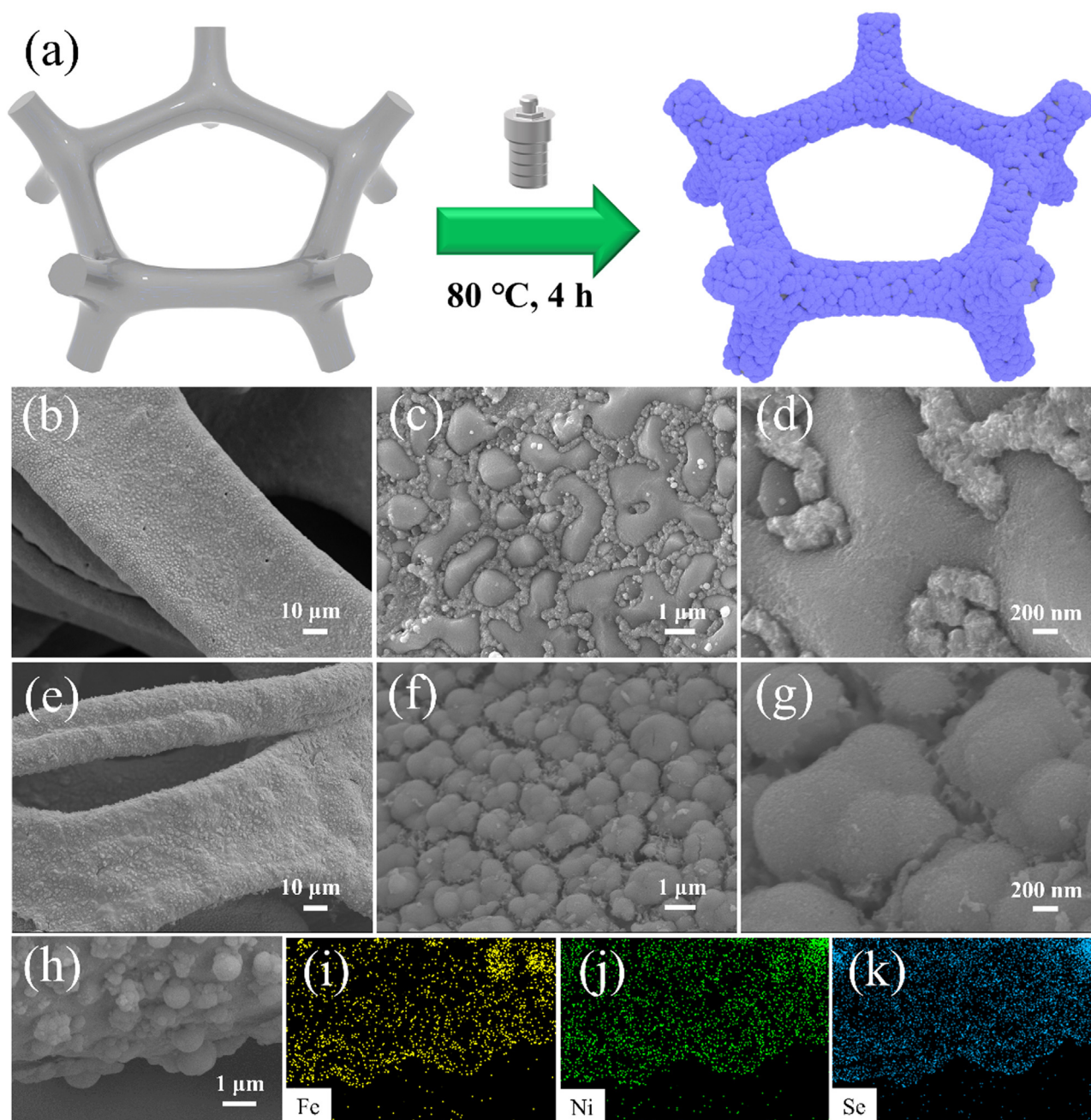


**Fig. 1.** (a) Preparation flow-chart of Fe-doped Ni<sub>0.85</sub>Se. SEM images of (b) Ni<sub>0.85</sub>Se/NF, (c) Fe-Ni<sub>0.85</sub>Se/NF at different magnifications, and (h)–(k) EDS elemental mapping of typical Fe-Ni<sub>0.85</sub>Se/NF.

S1). The corresponding electrochemical impedance spectroscopy (EIS) results at a fixed potential of 1.5 V were further explored (Fig. 4(c)). The  $R_{ct}$  of Fe-Ni<sub>0.85</sub>Se/NF was lower than those of Ni<sub>0.85</sub>Se/NF and RuO<sub>2</sub>/NF, indicating that Fe doping optimized the electron mass transfer rate. Double-layer capacitance ( $C_{dl}$ ) is an important index for evaluating the catalytic performance of a material. Figs. S5(a)(b) illustrate the cyclic voltammetry (CV) curves of different catalysts under different scanning rates within the 1.0–1.1 V range. The  $C_{dl}$  value of Fe-Ni<sub>0.85</sub>Se/NF (4.6 mF cm<sup>-2</sup>), as obtained from the CV curves, surpassed that of Ni<sub>0.85</sub>Se/NF (2.9 mF cm<sup>-2</sup>), further indicating that Fe introduction accelerates OER kinetics (Fig. S3(c)). As has been previously established, the electrochemical surface area (ECSA) has a linear relationship with  $C_{dl}$ . To verify the intrinsic activity of the catalyst, the current density of the OER polarization curve was normalized to the electrochemical

surface area. As shown in Fig. 4(d), Fe-Ni<sub>0.85</sub>Se/NF showed the highest current density under the same overpotential, indicating its higher intrinsic activity compared to those of Ni<sub>0.85</sub>Se/NF and RuO<sub>2</sub>/NF, while accentuating that Fe doping can effectively enhance the active center [45].

The corresponding LSV curves were obtained at a scanning rate of 1 mV s<sup>-1</sup> to examine the effect of temperature on catalytic performance. As depicted in Fig. S4(a), when 0.4 mmol Fe was quantitatively added, the catalyst prepared at 80 °C exhibited the highest catalytic performance with an overpotential of 276 mV at a current density of 100 mA cm<sup>-2</sup>, outperforming the catalysts prepared at 60 °C (292 mV) and 100 °C (286 mV). The above corroborates that temperature carries an important effect on the Fe doping process. In the catalyst synthesized at 60 °C, the 2p peak of Fe disappeared. At 80 °C, the ratio of Fe<sup>3+</sup>/Fe<sup>2+</sup>

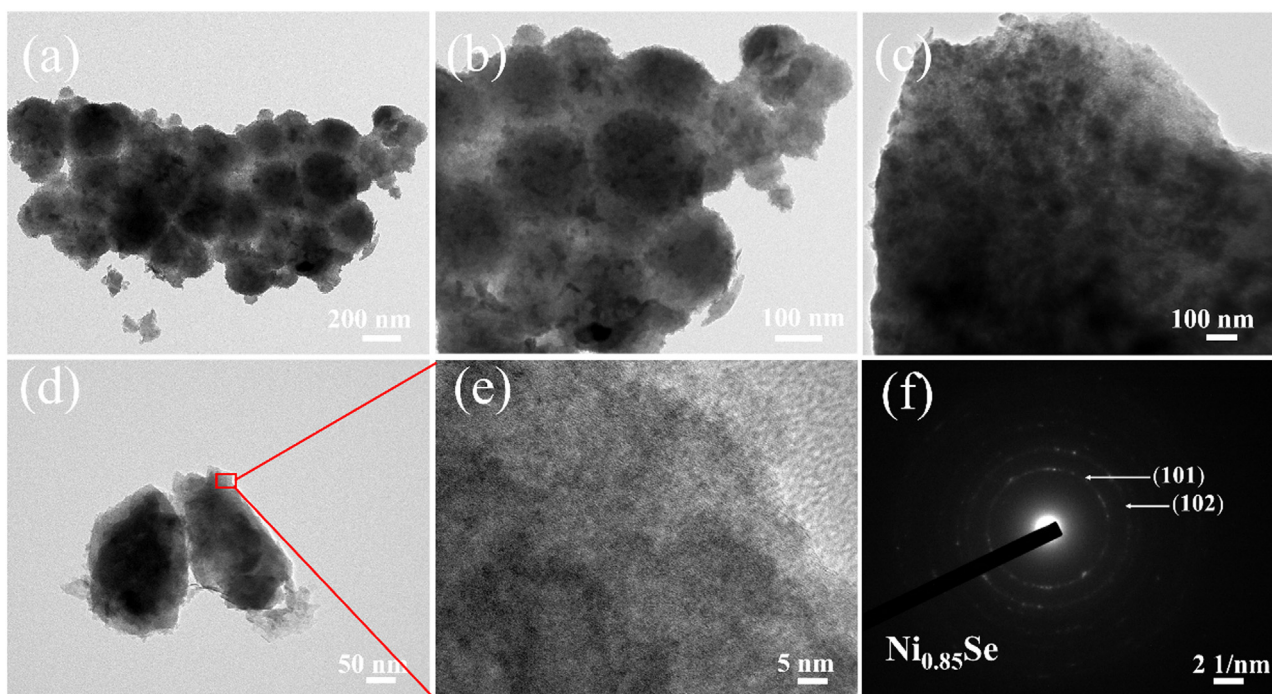


Fig. 2. (a)–(c) TEM images of typical Fe-Ni<sub>0.85</sub>Se/NF at different magnifications, (d)(e) high-magnification TEM images of Fe-Ni<sub>0.85</sub>Se/NF, and (f) corresponding SAED images of nanoparticles.

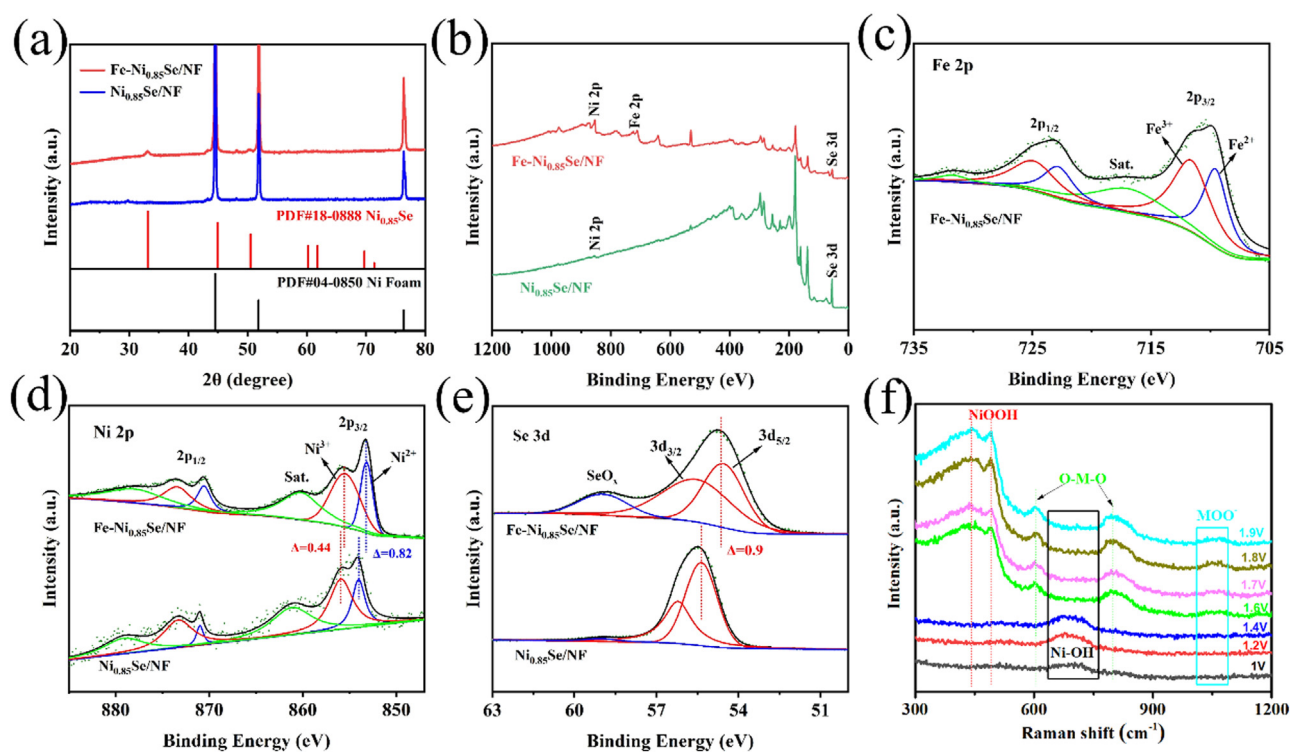
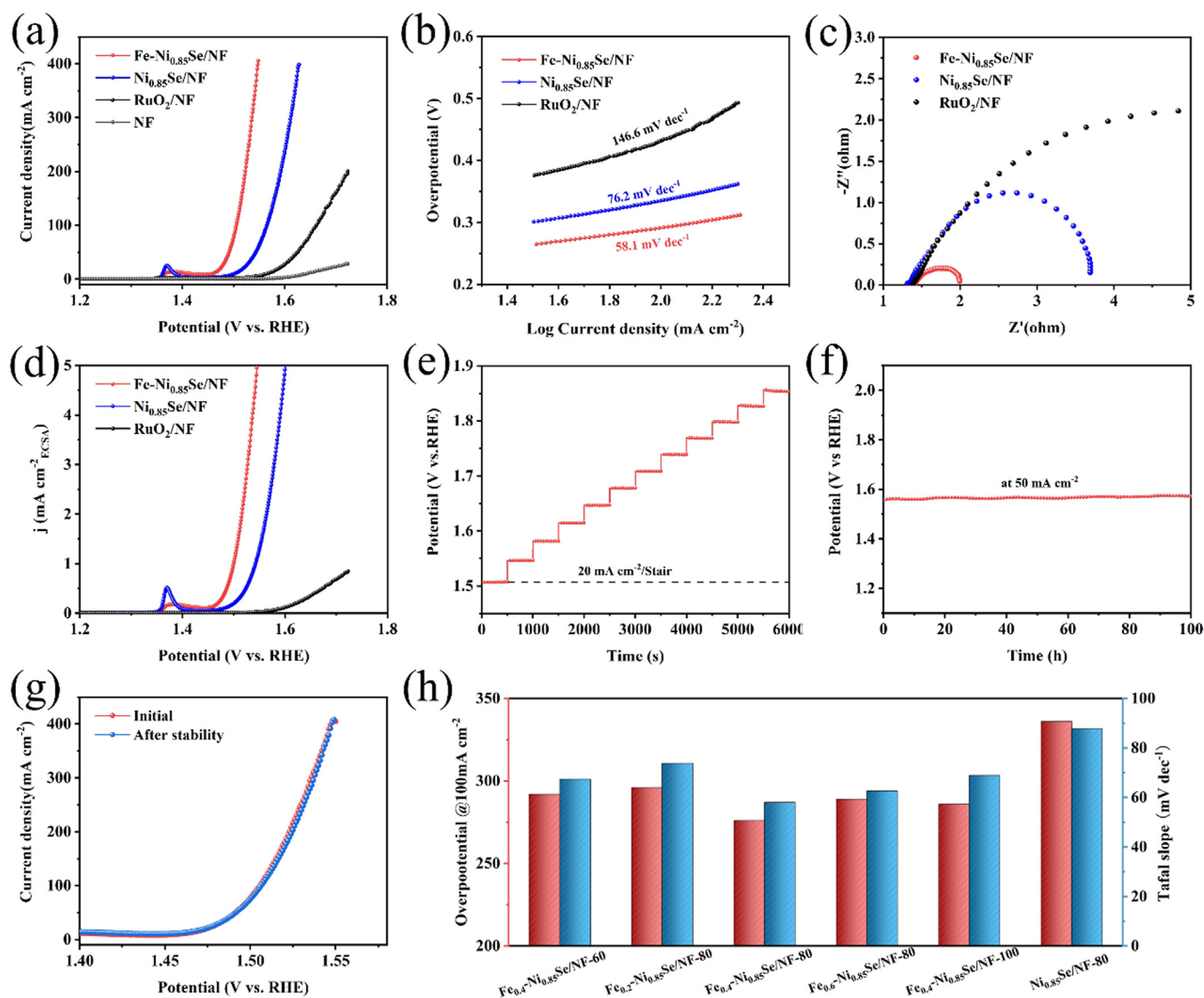


Fig. 3. (a) XRD patterns of Fe-Ni<sub>0.85</sub>Se/NF and Ni<sub>0.85</sub>Se/NF. (b) Full spectrum of Fe-Ni<sub>0.85</sub>Se/NF and Ni<sub>0.85</sub>Se/NF. Corresponding high-resolution XPS spectra of (c) Fe 2p, (d) Ni 2p, and (e) Se 3d. (f) In situ Raman spectra of Fe-Ni<sub>0.85</sub>Se/NF for the OER process in 0.1 M KOH solution.

was approximately 3:2, while at 100 °C, only the characteristic peak of Fe<sup>3+</sup> (Fig. S5) was observed. This suggested that the coexistence of Fe<sup>3+</sup> and Fe<sup>2+</sup> markedly enhanced the OER process. The Tafel slope of each electrolyte was calculated from its corresponding polarization curve (Fig. S4(b)). The smaller Tafel of Fe<sub>0.4</sub>-Ni<sub>0.85</sub>Se/NF-80 (58.1 mV dec<sup>-1</sup>) compared to those of Fe<sub>0.4</sub>-Ni<sub>0.85</sub>Se/NF-60 (67.4 mV dec<sup>-1</sup>) and Fe<sub>0.4</sub>-

Ni<sub>0.85</sub>Se/NF-100 (68.9 mV dec<sup>-1</sup>) highlighted that the temperature had a notable effect on the reaction kinetics. To illustrate the underlying mechanism of its excellent OER performance, the optimized catalyst underwent EIS analysis at a fixed potential of 1.5 V (Fig. S4(c)). Albeit not significantly different from those of Fe<sub>0.4</sub>-Ni<sub>0.85</sub>Se/NF-60 and Fe<sub>0.4</sub>-Ni<sub>0.85</sub>Se/NF-100, Fe<sub>0.4</sub>-Ni<sub>0.85</sub>Se/NF-80 demonstrated the small-



**Fig. 4.** (a) Linear sweep voltammetry and (b) corresponding Tafel slopes of typical samples (Fe-Ni<sub>0.85</sub>Se/NF, Ni<sub>0.85</sub>Se/NF, and commercial RuO<sub>2</sub>) in 1 M KOH. (c) Nyquist curve of typical sample at 1.5 V fixed potential. (d) OER performance of Fe-Ni<sub>0.85</sub>Se/NF, Ni<sub>0.85</sub>Se/NF, and RuO<sub>2</sub>/NF after the electrochemical surface area normalization. (e) Multistep chronopotentiometric curves of optimized Fe-Ni<sub>0.85</sub>Se/NF at different current densities (without iR compensation), (f) long-term CP curves of Fe-Ni<sub>0.85</sub>Se/NF measured at 50 mA cm<sup>-2</sup> for 100 h (without iR compensation) and (g) LSV curves of samples after long-term stability testing. (h) Performance comparison of oxygen evolution catalysts synthesized under different conditions.

est charge transfer resistance, indicating comparable electron transport rates. In addition, the  $C_{dl}$  values obtained from the CV curves gradually increased with a rise in temperature (Figs. S6 (a)–(d)).

Furthermore, the effects of different mole ratios of Fe doping on the characteristics at 80 °C were investigated. Fig. S7(a) illustrates the LSV curves. An overpotential of 296 mV was necessary for 0.2 mmol Fe doping to reach a current density of 100 mA cm<sup>-2</sup>, while Fe<sub>0.6</sub>-Ni<sub>0.85</sub>Se/NF-80 required 289 mV. As shown in Fig. S8, the XPS maps illustrate that Fe<sub>0.4</sub>-Ni<sub>0.85</sub>Se/NF-80 possessed the highest Fe<sup>3+</sup>/Fe<sup>2+</sup> ratio, followed by Fe<sub>0.6</sub>-Ni<sub>0.85</sub>Se/NF-80 and Fe<sub>0.2</sub>-Ni<sub>0.85</sub>Se/NF-80. The results indicated a close correlation between the Fe<sup>3+</sup>/Fe<sup>2+</sup> ratio and the OER performance, with performance improving as the ratio increased. This behavior stemmed from Fe<sup>3+</sup> exhibiting the best bonding energy for the adsorption of OER intermediates, which increased the catalyst's conductivity. Combined, these characteristics accelerated the electrode reaction kinetics. More importantly, Fe<sup>3+</sup> can act as a Lewis acid that oxidizes Fe<sup>3+</sup> and Ni<sup>3+</sup> cations during the catalytic process [46], ultimately producing highly active Ni<sup>4+</sup> species in the NiOOH matrix [47].

Therefore, the abundance of Fe<sup>3+</sup> ions favors the OER processes, as verified by the corresponding LSV curves (Fig. S7(a)). The Tafel slope of Fe<sub>0.4</sub>-Ni<sub>0.85</sub>Se/NF-80 (58.1 mV dec<sup>-1</sup>) was comparable to that of Fe<sub>0.6</sub>-Ni<sub>0.85</sub>Se/NF-80 (62.6 mV dec<sup>-1</sup>), with both being smaller than that of Fe<sub>0.2</sub>-Ni<sub>0.85</sub>Se/NF-80 (73.8 mV dec<sup>-1</sup>), indicating similar reaction kinetics (Fig. S7(b)). The corresponding EIS behavior at a fixed potential of 1.5 V was further investigated (Fig. S7(c)). Fe<sub>0.4</sub>-Ni<sub>0.85</sub>Se/NF-80 had the lowest charge transfer resistance compared to Fe<sub>0.2</sub>-Ni<sub>0.85</sub>Se/NF-80 and Fe<sub>0.6</sub>-Ni<sub>0.85</sub>Se/NF-80, demonstrating that the electron mass transfer rate is greatly affected by Fe doping. Furthermore, the  $C_{dl}$  increased as the Fe content increased (Figs. S9(a)–(d)).

Catalyst durability poses another crucial factor to consider when evaluating catalytic efficacy. The multistep chronopotentiometric (CP) curves of the conditioned Fe-Ni<sub>0.85</sub>Se/NF sample recorded without iR correction are shown in Fig. 4(e). The potential also increased and stabilized as the current density increased, demonstrating the remarkable electron mass transfer performance and mechanical stability of Fe-Ni<sub>0.85</sub>Se/NF. Furthermore, the CP curve of Fe-Ni<sub>0.85</sub>Se/NF at a current

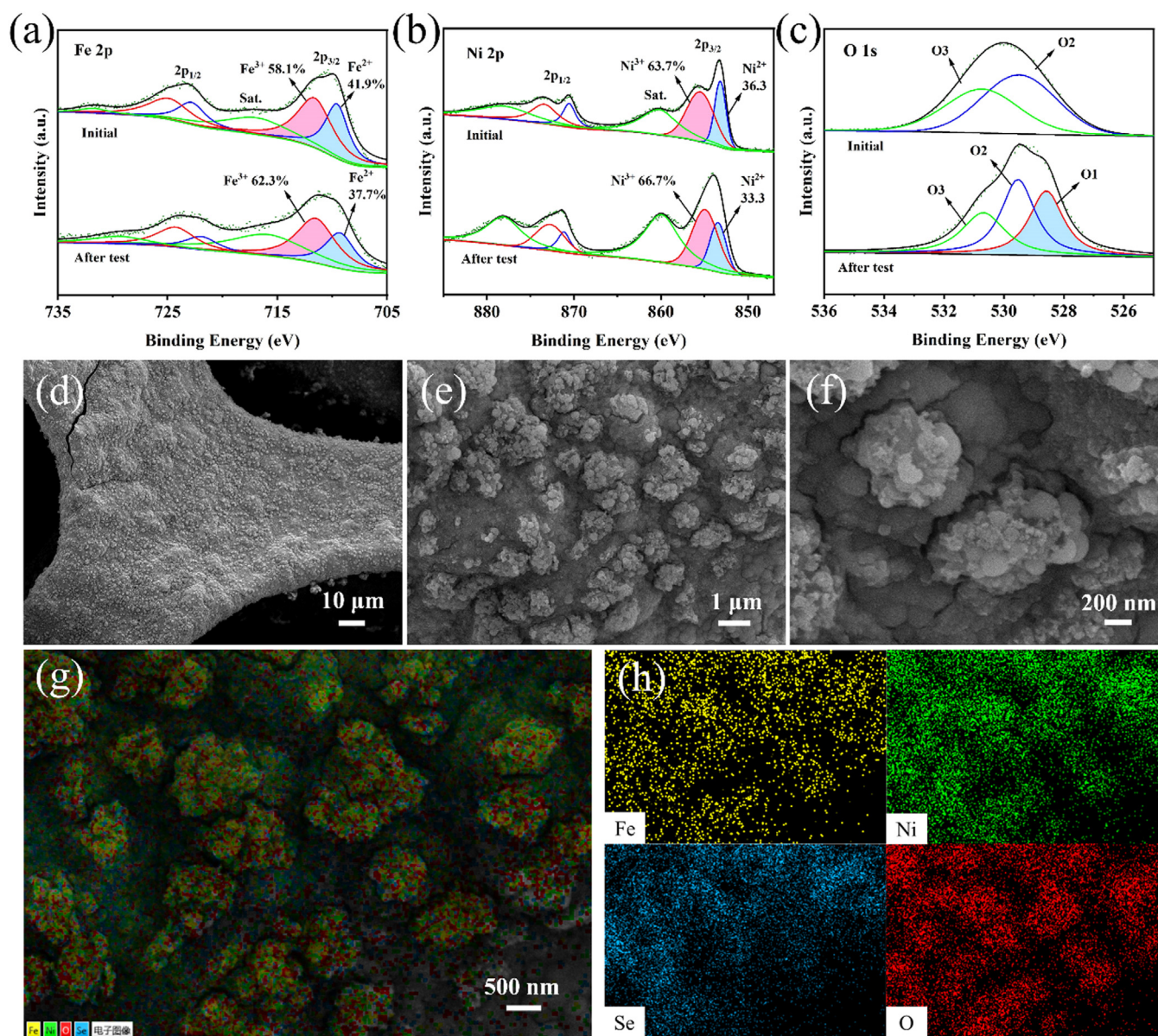


Fig. 5. High-resolution XPS spectra of (a) Fe 2p, (b) Ni 2p, and (c) O 1s before and after the stability test of Fe-Ni<sub>0.85</sub>Se/NF. (d)–(f) SEM diagram and (g)–(h) corresponding EDS element mapping after stability test.

density of 50 mA cm<sup>-2</sup> was evaluated for 100 h (Fig. 4(f)). The initial potential increased to 1.561 V without iR correction and to 1.572 V after 100 h of long-term testing. Further, the overpotential increased to approximately 11 mV. Moreover, the polarization curve generated by the catalyst shortly after the stability test nearly overlapped with that at the beginning (Fig. 4(g)), demonstrating outstanding OER stability. Fe-Ni<sub>0.85</sub>Se/NF exhibited excellent performance and stability, which can be attributed to the following factors: (1) the existence of multi-ionic valence Fe promoting the OER [48]; (2) the highly active Ni<sup>4+</sup> species formed in the structural transformation process owing to the synergistic effect of the Fe<sup>3+</sup> Lewis acid; (3) the synergistic effect of bimetallic Fe and Ni species on the OER process; (4) the enhanced coordination environment of Ni species as a result of Fe doping, which apart from improving the conductivity of the catalyst, it also positively modified its morphology by exposing additional active sites; and (5) the presence of the nickel foam conductive substrate, which enhanced the electron capture ability of Fe species, thereby improving their contribution to the OER.

The structure of the catalysts transformed after the OER test conducted herein, which has also been confirmed in several previous reports [49–51]. Figs. 5(a)–(c) show the XPS spectra of Fe-Ni<sub>0.85</sub>Se/NF before and after the stability tests. Following the OER test, the ratio of Fe<sup>3+</sup>/Fe<sup>2+</sup> and Ni<sup>3+</sup>/Ni<sup>2+</sup> both increased. This was attributed to the electrophilic \*O (\* represents the adsorption center) in the OER process restructuring a part of the surface of Fe-Ni<sub>0.85</sub>Se/NF into MOOH (M = Fe, Ni) through a nucleophilic attack, which has been confirmed to substantially enhance the catalytic activity in the OER process [52,53]. The XPS profiles of the catalysts were recorded before and after the test (Fig. 5(c)). Before the OER test, the O 1s peaks can be deconvoluted into defective oxygen (O<sub>2</sub>) at 529.5 eV and adsorbed oxygen (O<sub>3</sub>) at 530.8 eV. Nevertheless, after the OER test, they can be deconvoluted into metal-oxygen (O<sub>1</sub>) at 528.5 eV, defect oxygen (O<sub>2</sub>) at 529.5 eV, and adsorbed oxygen (O<sub>3</sub>) at 530.7 eV. The emergence of O<sub>1</sub> confirmed the occurrence of structural transformation in the Fe and Ni species during the OER, with MOOH (M = Fe, Ni) being the likely cause of the O<sub>1</sub> peak appearance. The change in the surface morphology further indi-

cated this transformation, which was also observed in the in-situ Raman spectra depicted in Fig. 3(f). As shown in Figs. 5(d)(e), the catalyst surface underwent limited morphological changes, and some originally large particles changed into irregular small particle aggregates, demonstrating that the metal active center was transformed into amorphous MOOH at the initial OER stage. Parallely, EDS elemental mapping was performed post-OER process to confirm the presence of elements before the OER (Figs. 5(g)(h)). The results demonstrated an even distribution of Fe, Ni, and Se elements, further accentuating the excellent stability of the catalyst. Compared to the pre-OER test, O was evenly distributed, as expected; however, the Fe/Ni ratio and Fe species content decreased (Fig. S10). As reported previously [41], the strong interaction between Fe and \*O was responsible for the collapse of the Fe species, resulting in a lower Fe/Ni ratio after the completion of the OER test [54].

### 3. Conclusions

In conclusion, Fe-doped NiSe compounds with remarkable OER performance and stability were synthesized via ion etching using a straightforward one-step hydrothermal method without exogenous Ni salts. Fe doping induced changes in the local coordination environment and surface morphology of the Ni species, exposing more active sites. The presence of polyvalent Fe ions facilitated the adsorption of \*O by the Ni species, promoting structural transformation during the OER and enhancing activity. Additionally, the Lewis acidity of Fe<sup>3+</sup> contributed to the oxidation of Ni species to Ni<sup>4+</sup>, further boosting catalytic activity. Overall, Fe-doping significantly enhances the OER properties of NiSe compounds. Interestingly, the optimized Fe-Ni<sub>0.85</sub>Se/NF exhibited outstanding performance with an overpotential of 276 mV at a current density of 100 mA cm<sup>-2</sup>, maintaining high performance throughout a 100 h OER test. This study presents a straightforward and successful methodology for developing non-noble metal catalysts while streamlining the synthesis steps and reducing experimental costs.

### Declaration of Competing Interest

The authors declare that they have no known competing financial interests or personal relationships that could have appeared to influence the work reported in this paper.

### CRedit authorship contribution statement

**Longqi Zhu:** Writing – original draft, Conceptualization. **Runze Wang:** Investigation, Data curation. **Chen Wang:** Methodology, Formal analysis. **Shuhan Yang:** Validation, Formal analysis. **Haizhen Liu:** Validation, Funding acquisition. **Bo Xing:** Writing – original draft, Funding acquisition. **Honghui Cheng:** Data curation. **Kuikui Wang:** Writing – review & editing, Funding acquisition.

### Acknowledgements

The authors acknowledge the financial support provided by the National Natural Science Foundation of China (51801108), the Shandong Provincial Natural Science Foundation (ZR2023ME072), and the Key Research and Development Program of Shandong Province (2019GGX103048). Additionally, this project received support from the Jiangsu Key Laboratory of Advanced Catalytic Materials and Technology (BM2012110), the Open Foundation of Guangxi Key Laboratory of Processing for Non-Ferrous Metals and Featured Materials (2022GXYSOF16), and the Open Foundation of the National Engineering Laboratory of Circular Economy at Sichuan University of Science and Engineering (XHJJ-2304).

### Supplementary materials

Supplementary material associated with this article can be found, in the online version, at doi:10.1016/j.chphma.2024.03.002.

### References

- J. Pan, Y. Fu, G. Xiao, J. Niu, J. Cao, J. Wang, Y. Zheng, C. Li, Photocatalytic overall water splitting hydrogen evolution enhancement of ZnO nanoarrays/LaCrO<sub>3</sub> film heterojunction via HER/OER synergism of CoP/FTO, *J. Environ. Chem. Eng.* 10 (2022) 108587, doi:10.1016/j.jece.2022.108587.
- M. Usman, Z. Zeb, H. Ullah, H.S. Munzir, H. Muhammad, U. Latif, N.A.S. Syed, A. Usama, S. Muhammad, A review of metal-organic frameworks/graphitic carbon nitride composites for solar-driven green H<sub>2</sub> production, CO<sub>2</sub> reduction, and water purification, *J. Environ. Chem. Eng.* 10 (2022) 107548, doi:10.1016/j.jece.2022.107548.
- J. Chang, Z. Hu, D. Wu, F. Xu, C. Chen, K. Jiang, Z. Gao, Prussian blue analog-derived nickel iron phosphide-reduced graphene oxide hybrid as an efficient catalyst for overall water electrolysis, *J. Colloid Interf. Sci.* 638 (2023) 801–812, doi:10.1016/j.jcis.2023.02.037.
- Z. Li, X. Wang, X. Wang, Y. Lin, A. Meng, L. Yang, Q. Li, Mn-Cd-S@amorphous-Ni<sub>3</sub>S<sub>2</sub> hybrid catalyst with enhanced photocatalytic property for hydrogen production and electrocatalytic OER, *Appl. Surf. Sci.* 491 (2019) 799–806, doi:10.1016/j.apsusc.2019.05.313.
- L. Zhu, Y. Liao, Y. Jia, X. Zhang, R. Ma, K. Wang, Solid-solution hexagonal Ni<sub>0.5</sub>Co<sub>0.5</sub>Se nanoflakes toward the boosted oxygen evolution reaction, *Chem. Commun.* 56 (2020) 13113–13116, doi:10.1039/D0CC05247G.
- L. Jin, C. Liu, D. Wang, M. Liu, T.G. Lee, S.G. Peera, X. Qi, CdN<sub>4</sub>C<sub>6</sub>-gra as efficient trifunctional electrocatalyst for the HER, OER and ORR: A density functional theory study, *Appl. Surf. Sci.* 610 (2023) 155580, doi:10.1016/j.apsusc.2022.155580.
- D. Chen, Q. Sun, C. Han, Y. Guo, Q. Huang, W.A. Goddard, J. Qian, Enhanced oxygen evolution catalyzed by in situ formed Fe-doped Ni oxyhydroxides in carbon nanotubes, *J. Mater. Chem. A* 10 (2022) 16007–16015, doi:10.1039/D2TA04042E.
- T. Tang, S. Jiao, Ji. Han, Z. Wang, J. Guan, Partially crystallized Ni-Fe oxyhydroxides promotes oxygen evolution, *Int. J. Hydrog. Energ.* 48 (2023) 5774–5782, doi:10.1016/j.ijhydene.2022.11.118.
- L. Tabassum, M.K. Islam, I.P. Perera, M. Li, X. Huang, H. Tasnim, S.L. Suib, Facile synthesis of transition-metal-doped (Fe, Co, and Ni) CuS/CuO/CS nanorod arrays for superior electrocatalytic oxygen evolution reaction, *ACS Appl. Energy Mater.* 5 (2022) 12039–12048, doi:10.1021/acsaelm.2c01384.
- C. Li, L. Xie, J. Zhao, L. Gu, J. Wu, G. Li, Interfacial electronic modulation by Fe<sub>2</sub>O<sub>3</sub>/NiFe-LDHs heterostructures for efficient oxygen evolution at high current density, *Appl. Catal. B: Environ.* 306 (2022) 121097, doi:10.1016/j.apcatb.2022.121097.
- T. Tang, Z. Wang, J. Guan, A review of defect engineering in two-dimensional materials for electrocatalytic hydrogen evolution reaction, *Chin. J. Catal.* 43 (2022) 636–678, doi:10.1016/S1872-2067(21)63945-1.
- K. Zhang, R. Zou, Advanced transition metal-based OER electrocatalysts: Current status, opportunities, and challenges, *Small* 17 (2021) 2100129, doi:10.1002/smll.202100129.
- Y. Pan, J. Gao, E. Lv, T. Li, H. Xu, L. Sun, A. Nairan, Q. Zhang, Integration of alloy segregation and surface Co-O Hybridization in carbon-encapsulated CoNiPt alloy catalyst for superior alkaline hydrogen evolution, *Adv. Funct. Mater.* 33 (2023) 202303833, doi:10.1002/adfm.202303833.
- T. Wang, P. Wang, W. Zang, X. Li, D. Chen, Z. Kou, S. Mu, J. Wang, Nanoframes of Co<sub>3</sub>O<sub>4</sub>-Mo<sub>2</sub>N heterointerfaces enable high-performance bifunctionality toward both electrocatalytic HER and OER, *Adv. Funct. Mater.* 32 (2022) 2107382, doi:10.1002/adfm.202107382.
- J. Zhang, J. Lian, Q. Jiang, G. Wang, Boosting the OER/ORR/HER activity of Ru-doped Ni/Co oxides heterostructure, *Chem. Eng. J.* 439 (2022) 135634, doi:10.1016/j.cej.2022.135634.
- M.K. Debe, Electrocatalyst approaches and challenges for automotive fuel cells, *Nature* 486 (2012) 43–51, doi:10.1038/nature11115.
- J. Guan, X. Bai, T. Tang, Recent progress and prospect of carbon-free single-site catalysts for the hydrogen and oxygen evolution reactions, *Nano Res.* 15 (2022) 818–837, doi:10.1007/s12274-021-3680-9.
- S. Anantharaj, V. Aravindan, Developments and perspectives in 3D transition-metal-based electrocatalysts for neutral and near-neutral water electrolysis, *Adv. Energy Mater.* 10 (2020) 1902666, doi:10.1002/aenm.201902666.
- L. Zhang, W. Cai, N. Bao, H. Yang, Implanting an electron donor to enlarge the d-p hybridization of high-entropy (oxy) hydroxide: A novel design to boost oxygen evolution, *Adv. Mater.* 34 (2022) 2110511, doi:10.1002/adma.202110511.
- X. Bai, L. Wang, B. Nan, T. Tang, X. Niu, J. Guan, Atomic manganese coordinated to nitrogen and sulfur for oxygen evolution, *Nano Res.* 15 (2022) 6019–6025, doi:10.1007/s12274-022-4293-7.
- L. Li, X. Cao, J. Huo, J. Qu, W. Chen, C. Liu, Y. Zhao, H. Liu, G. Wang, High valence metals engineering strategies of Fe/Co/Ni-based catalysts for boosted OER electrocatalysis, *J. Energy Chem.* 76 (2022) 195–213, doi:10.1016/j.jechem.2022.09.022.
- Z. Feng, T. Shi, W. Liu, W. Zhang, H. Zhang, Highly active bifunctional electrocatalyst: Nanoporous (Ni, Co)<sub>0.85</sub>Se anchored on rGO for water and hydrazine oxidation, *Int. J. Energ. Res.* 46 (2022) 15938–15947, doi:10.1002/er.8292.
- J. Han, J. Guan, Multicomponent transition metal oxides and (oxy) hydroxides for oxygen evolution, *Nano Res.* 16 (2022) 1–54, doi:10.1007/s12274-022-4874-7.
- T. Guo, L. Li, Z. Wang, Recent development and future perspectives of amorphous transition metal-based electrocatalysts for oxygen evolution reaction, *Adv. Energy Mater.* 12 (2022) 202200827, doi:10.1002/aenm.202200827.
- H. Singh, R. Biswas, I. Ahmed, P. Thakur, A. Kundu, A.R. Panigrahi, B. Banerjee, K.K. Halder, J. Lahtinen, K. Mondal, K.K. Haldar, Dumbbell-shaped ternary transition-metal (Cu, Ni, Co) phosphate bundles: a promising catalyst for the oxygen evolution reaction, *ACS Appl. Mater. Interface.* 14 (2022) 6570–6581, doi:10.1021/acsami.1c20356.
- P. Bhanja, Y. Kim, B. Paul, J. Lin, S.M. Alshehri, T. Ahamad, Y.V. Kaneti,

- A. Bhaumik, Y. Yamauchi, Facile synthesis of nanoporous transition metal-based phosphates for oxygen evolution reaction, *ChemCatChem* 12 (2020) 2091–2096, doi:10.1002/cctc.201901803.
- [27] Y. Zhang, R. Wang, L. Zhu, X. Li, C. Sun, H. Liu, L. Zhu, K. Wang, Carbon quantum dots-Doped Ni<sub>3</sub>Se<sub>4</sub>/Co<sub>3</sub>Se<sub>3</sub>/Fe<sub>3</sub>O<sub>4</sub> multilayer nanosheets prepared using the one-step solvothermal method to boost electrocatalytic oxygen evolution, *Mater. (Basel)* 14 (2023) 5115, doi:10.3390/ma16145115.
- [28] T. Zhang, J. Sun, J. Guan, Self-supported transition metal chalcogenides for oxygen evolution, *Nano Res.* 16 (2023) 8684–8711, doi:10.1007/s12274-023-5670-6.
- [29] J. Zhao, L. Yang, H. Li, T. Huang, H. Cheng, A. Meng, Y. Lin, P. Wu, X. Yuan, Z. Li, Ni<sub>3</sub>Se<sub>2</sub> nanosheets in-situ grown on 3D NiSe nanowire arrays with enhanced electrochemical performances for supercapacitor and efficient oxygen evolution, *Mater. Charact.* 172 (2021) 110819, doi:10.1016/j.matchar.2020.110819.
- [30] C. Yang, Y. Lu, W. Duan, Z. Kong, C. Li, Huang, T. Yang, Y. Zou, R. Chen, S. Wang, Recent progress and prospective of nickel selenide-based electrocatalysts for water splitting, *Energ. Fuel.* 35 (2021) 14283–14303, doi:10.1021/acs.energyfuels.1c01854.
- [31] D. Chen, Y. Chen, W. Zhang, R. Cao, Nickel selenide from single-molecule electrodeposition for efficient electrocatalytic overall water splitting, *New. J. Chem.* 45 (2021) 351–357, doi:10.1039/D0NJ04966B.
- [32] Y. Li, R. Chen, D. Yan, S. Wang, Regulation of morphology and electronic structure of NiSe<sub>2</sub> by Fe for high effective oxygen evolution reaction, *Chem.-Asian J.* 15 (2020) 3845–3852, doi:10.1002/asia.202000860.
- [33] C. Zhang, Y. Zhang, S. Zhou, C. Li, Self-supported iron-doping NiSe<sub>2</sub> nanowrinkles as bifunctional electrocatalysts for electrochemical water splitting, *J. Alloy. Compd.* 818 (2020) 152833, doi:10.1016/j.jallcom.2019.152833.
- [34] X. Zhang, H. Pan, Y. Jia, Y. Zhang, Z. Jiang, C. Li, X. Li, L. Bao, R. Ma, K. Wang, Flower-like MOF-74 nanocomposites directed by selenylation towards high-efficient oxygen evolution, *J. Colloid Interf. Sci.* 623 (2022) 552–560, doi:10.1016/j.jcis.2022.04.181.
- [35] K. Guo, Y. Wang, S. Yang, J. Huang, Z. Zou, H. Pan, P.S. Shinde, S. Pan, J. Huang, C. Xu, Bonding interface boosts the intrinsic activity and durability of NiSe@Fe<sub>2</sub>O<sub>3</sub> heterogeneous electrocatalyst for water oxidation, *Sci. Bull.* 66 (2021) 52–61, doi:10.1016/j.scib.2020.06.003.
- [36] D. Liang, J. Mao, P. Liu, J. Li, J. Yan, W. Song, In-situ doping of Co in nickel selenide nanoflower for robust electrocatalysis towards oxygen evolution, *Int. J. Hydrog. Energ.* 45 (2020) 27047–27055, doi:10.1016/j.ijhydene.2020.07.017.
- [37] T. Wang, D. Gao, W. Xiao, P. Xi, D. Xue, J. Wang, Transition-metal-doped NiSe<sub>2</sub> nanosheets towards efficient hydrogen evolution reactions, *Nano Res.* 11 (2018) 6051–6061, doi:10.1007/s12274-018-2122-9.
- [38] K. Chang, D.T. Tran, J. Wang, N.H. Kim, J.H. Lee, A 3D hierarchical network derived from 2D Fe-doped NiSe nanosheets/carbon nanotubes with enhanced OER performance for overall water splitting, *J. Mater. Chem. A* 10 (2022) 3102–3111, doi:10.1039/D1TA07393A.
- [39] Y. Liu, J. Cao, Y. Chen, M. Wei, X. Liu, X. Li, Q. Wu, B. Feng, Y. Zhang, L. Yang, Regulation of the morphology and electrochemical properties of Ni<sub>0.85</sub>Se via Fe doping for overall water splitting and supercapacitors, *Cryst. Eng. Comm.* 24 (2022) 1704–1718, doi:10.1039/D1CE01555A.
- [40] G. Liu, C. Shuai, Z. Mo, R. Guo, N. Liu, Q. Dong, J. Wang, H. Pei, W. Liu, X. Guo, Fe-doped Ni<sub>0.85</sub>Se nanospheres interspersed into carbon nanotubes as efficient and stable electrocatalyst for overall water splitting, *Electrochim. Acta* 385 (2021) 138452, doi:10.1016/j.electacta.2021.138452.
- [41] Y. Zhang, L. You, Q. Liu, Y. Li, T. Li, Z. Xue, G. Li, Interfacial charge transfer in a hierarchical Ni<sub>2</sub>P/FeOOH heterojunction facilitates electrocatalytic oxygen evolution, *ACS Appl. Mater. Interface.* 13 (2021) 2765–2771, doi:10.1021/acsami.0c20204.
- [42] W. Zhou, Z. Xue, Q. Liu, Y. Li, J. Hu, G. Li, Trimetallic MOF-74 films grown on Ni foam as bifunctional electrocatalysts for overall water splitting, *ChemSusChem* 13 (2020) 5647–5653, doi:10.1002/cssc.202001230.
- [43] S. Niu, W. Jiang, T. Tang, L. Yuan, H. Luo, J. Hu, Autogenous growth of hierarchical NiFe(OH)<sub>2</sub>/FeS nanosheet-on-microsheet arrays for synergistically enhanced high-output water oxidation, *Adv. Funct. Mater.* 29 (2019) 201902180, doi:10.1002/adfm.201902180.
- [44] X. Xia, G. Zhao, Q. Yan, B. Wang, Q. Wang, H. Xie, High-density defects activating Fe-doped molybdenum sulfide @N-doped carbon heterostructures for efficient electrochemical hydrogen evolution, *ACS Sustain. Chem. Eng.* 10 (2021) 182–193, doi:10.1021/acssuschemeng.1c05538.
- [45] Z. Xue, X. Li, Q. Liu, M. Cai, K. Liu, M. Liu, Z. Ke, X. Liu, G. Li, Interfacial electronic structure modulation of NiTe nanoarrays with NiS nanodots facilitates electrocatalytic oxygen evolution, *Adv. Mater.* 31 (2019) 1900430, doi:10.1002/adma.201900430.
- [46] H. Pan, X. Zhang, Y. Jia, Y. Zhang, Z. Jiang, C. Sun, X. Li, L. Zhu, K. Wang, Interfacial composite FeOOH enhanced efficient electrocatalytic oxygen evolution of NiSe<sub>2</sub>/Ni<sub>2</sub>O<sub>3</sub>, *J. Alloy. Compd.* 926 (2022) 166779, doi:10.1016/j.jallcom.2022.166779.
- [47] S. Anantharaj, S. Kundu, S. Noda, The Fe effect: A review unveiling the critical roles of Fe in enhancing OER activity of Ni and Co based catalysts, *Nano Energy* 80 (2021) 105514, doi:10.1016/j.nanoen.2020.105514.
- [48] X. Meng, J. Han, L. Lu, G. Qiu, Z. Wang, C. Su, Fe<sup>2+</sup>-doped layered double (Ni, Fe) hydroxides as efficient electrocatalysts for water splitting and self-powered electrochemical systems, *Small* 15 (2019) 1902551, doi:10.1002/smll.201902551.
- [49] S. Zhao, C. Tan, C. He, P. An, F. Xie, S. Jiang, Y. Zhu, K. Wu, B. Zhang, H. Li, J. Zhang, Y. Chen, S. Liu, J. Dong, Z. Tang, Structural transformation of highly active metal-organic framework electrocatalysts during the oxygen evolution reaction, *Nat. Energy* 5 (2020) 881–890, doi:10.1038/s41560-020-00709-1.
- [50] G. Solomon, A. Landström, R. Mazzaro, M. Jugovac, P. Moras, E. Cattaruzza, V. Morandi, I. Concina, A. Vomiero, NiMoO<sub>4</sub>@Co<sub>3</sub>O<sub>4</sub> core-shell nanorods: In situ catalyst reconstruction toward high efficiency oxygen evolution reaction, *Adv. Energy Mater.* 11 (2021) 2101324, doi:10.1002/aenm.202101324.
- [51] Z. Tan, L. Sharma, R. Kakkar, T. Meng, Y. Jiang, M. Cao, Arousing the reactive Fe sites in pyrite (FeS<sub>2</sub>) via integration of electronic structure reconfiguration and in situ electrochemical topotactic transformation for highly efficient oxygen evolution reaction, *Inorg. Chem.* 58 (2019) 7615–7627, doi:10.1021/acs.inorgchem.9b01017.
- [52] B. Wu, S. Gong, Y. Lin, T. Li, A. Chen, M. Zhao, Q. Zhang, L. Chen, A unique NiOOH@FeOOH heteroarchitecture for enhanced oxygen evolution in saline water, *Adv. Mater.* 34 (2022) 2108619, doi:10.1002/adma.202108619.
- [53] K. Wan, J. Luo, C. Zhou, T. Zhang, J. Arbiol, X. Lu, B. Mao, X. Zhang, J. Fransaer, Hierarchical porous Ni<sub>3</sub>S<sub>4</sub> with enriched high-valence Ni sites as a robust electrocatalyst for efficient oxygen evolution reaction, *Adv. Funct. Mater.* 29 (2019) 1900315, doi:10.1002/adfm.201900315.
- [54] Z. Wu, H. Zhang, S. Zuo, Y. Wang, S.L. Zhang, J. Zhang, S. Zang, X.W.D. Lou, Manipulating the local coordination and electronic structures for efficient electrocatalytic oxygen evolution, *Adv. Mater.* 33 (2021) 2103004, doi:10.1002/adma.202103004.